

Cite this: *Nanoscale*, 2016, 8, 2727

# Facile synthesis of SnO<sub>2</sub>–PbS nanocomposites with controlled structure for applications in photocatalysis†

Arik Kar,<sup>a</sup> Sumanta Sain,<sup>b</sup> David Rossouw,<sup>a,c</sup> Benjamin R. Knappett,<sup>a</sup> Swapan Kumar Pradhan<sup>b</sup> and Andrew E. H. Wheatley<sup>\*a</sup>

Recent studies have shown that SnO<sub>2</sub>-based nanocomposites offer excellent electrical, optical, and electrochemical properties. In this article, we present the facile and cost-effective fabrication, characterization and testing of a new SnO<sub>2</sub>–PbS nanocomposite photocatalyst designed to overcome low photocatalytic efficiency brought about by electron–hole recombination and narrow photoresponse range. The structure is fully elucidated by X-ray diffraction (XRD)/Reitveld refinement, Raman spectroscopy, X-ray photoelectron spectroscopy (XPS), Brunauer–Emmett–Teller (BET) surface area analysis, and transmission electron microscopy (TEM). Energy-dispersive X-ray spectroscopy (EDX) spectrum imaging analysis demonstrates the intermixing of SnO<sub>2</sub> and PbS to form nanocomposites. A charge separation mechanism is presented that explains how the two semiconductors in junction function synergistically. The efficacy of this new nanocomposite material in the photocatalytic degradation of the toxic dye Rhodamine B under simulated solar irradiation is demonstrated. An apparent quantum yield of 0.217 mol min<sup>−1</sup> W<sup>−1</sup> is calculated with data revealing good catalyst recyclability and that charge separation in SnO<sub>2</sub>–PbS leads to significantly enhanced photocatalytic activity in comparison to either SnO<sub>2</sub> or PbS.

Received 11th October 2015,  
Accepted 12th December 2015

DOI: 10.1039/c5nr07036h

www.rsc.org/nanoscale

## Introduction

The term ‘nanocomposite’ is used to describe a multiphase solid material in which one of the phases has one, two or three dimensions of less than 100 nm.<sup>1</sup> Nanocomposites frequently exhibit properties (or a combination of properties) not available through any of the components in the composite individually. The fabrication of nanocomposite materials therefore promises access to previously unachievable properties of technological importance in applications<sup>2</sup> including LEDs, lasers, non-linear optical devices<sup>3</sup> and bio-labelling.<sup>4</sup> In the specific contexts of electrochemistry/photochemistry/photophysics and photoelectrochemistry/photocatalysis, nanocomposite materials have been extensively utilized.<sup>5</sup> The unique properties of the nanocomposite materials are generally considered to arise from the interfacial interactions of

their component phases,<sup>6</sup> with two boundary cases recognized in nanocomposites. The first involves covalent interactions, which seldom form spontaneously, but can be created by particular surface treatments.<sup>7</sup> The second involves van der Waals interactions.<sup>6</sup> In practice the strength of interfacial interactions are somewhere between these two boundary extremes.<sup>8</sup> The unique, size-dependent physical and chemical properties of nanocomposite materials, combined with their high processability and defined chemical and morphological structures, which frequently present unique and tunable characteristics, cannot be achieved by traditional core-shell or heterodimer structure nanomaterials.<sup>9</sup>

A field that has received significant attention over the last two decades is that of nanocomposites comprising two semiconductors with different band gaps. Such semiconductor-based nanocomposites exhibit properties derived from the interfacial interactions of their component phases. Additionally, size-quantized optical and optoelectronic effects bring an innovative dimension to research as both the photonic characteristics of semiconductor particles are significantly modified in the (sub-)nanometer regime.<sup>10,11</sup> One consequence of this is that nanocomposites of semiconductor materials are attracting considerable attention in the context of developing devices such as light emitting diodes and solar cells,<sup>12–14</sup> solar photovoltaic devices and chemical/biological sensors.<sup>15</sup>

<sup>a</sup>Department of Chemistry, University of Cambridge, Lensfield Road, Cambridge, CB2 1EW, UK. E-mail: aehw2@cam.ac.uk; Tel: +44 (0)1223 (7)63966

<sup>b</sup>Materials Science Division, Department of Physics, The University of Burdwan, Golapbag, Burdwan, West Bengal 713 104, India

<sup>c</sup>Department of Materials Science and Engineering, Brockhouse Institute for Materials Research and Canadian Centre for Electron Microscopy, McMaster University, Hamilton, Ontario, L8S 4L8, Canada

†Electronic supplementary information (ESI) available. See DOI: 10.1039/c5nr07036h

A significant number of semiconductor-based nanocomposites have been reported.<sup>5</sup> Central to the present study are systems based on  $\text{SnO}_2$ . These have the advantages that  $\text{SnO}_2$  is a stable oxide semiconductor with a wide n-type band gap of 3.6 eV (ref. 16) and that it is both low cost and non-toxic.  $\text{SnO}_2$  has been applied in the fields of solar cells,<sup>17</sup> catalytic support materials,<sup>18</sup> transparent electrodes,<sup>19</sup> and solid-state chemical sensors.<sup>20</sup> Recent years have seen efforts to control the synthesis of  $\text{SnO}_2$ -semiconductor nanocomposites in which the valence band and conduction band positions have been modulated in an attempt to increase the carrier lifetime of photolytically induced electrons and holes. For example, Zhang *et al.*<sup>21</sup> prepared  $\text{SnO}_2$ - $\text{Ag}_3\text{PO}_4$  semiconductor nanocomposites which exhibit much higher photocatalytic activity and improved stability relative to pure  $\text{Ag}_3\text{PO}_4$  or  $\text{SnO}_2$ , while McCue *et al.*<sup>22</sup> synthesized  $\text{SnO}_2$ - $\text{In}_2\text{O}_3$  nanocomposites that exhibited outstanding sensitivity for both reducing and oxidizing gases. Pan *et al.*<sup>23</sup> have suggested that  $\text{SnO}_2$ -CdS nanocomposites exhibit promise for highly sensitive visible-light photodetectors and efficient photocatalysis. A nanocomposite of iron(III) oxide and tin(IV) oxide, 50:50  $\text{SnO}_2$ - $\text{Fe}_2\text{O}_3$  was prepared by Tai *et al.*<sup>24</sup> and revealed excellent electrocatalytic activity towards the oxidation of epinephrine, acetaminophen and tryptophan.  $\text{SnO}_2$  has also demonstrated the ability to mix with carbon nanotubes,<sup>25</sup> carbon,<sup>26</sup> and with reduced graphene oxide<sup>27</sup> to form  $\text{SnO}_2$ -based nanocomposites.

$\text{SnO}_2$ -based nanocomposites containing PbS as the other active component are, to the best of our knowledge, unreported. Such a combination would be extremely desirable, there being a large band gap difference (approximately 3.2 eV) between the two component materials. This offers increased charge separation and promises enhanced electrical, optical, electrochemical, photocatalytic and gas sensing properties. PbS itself is a metal sulfide semiconductor with a narrow bulk bandgap of 0.41 eV at room temperature<sup>28</sup> that has applications in fiber optics, telecommunications, lasers, solar cells and biological systems.<sup>29</sup> It is established that the optical, electronic and magnetic properties of PbS nanocrystals significantly differ from those of bulk PbS, the band gaps of PbS nanocrystals being significantly blue shifted from the near-IR into the visible and near-UV regions with decreasing particle size.<sup>30</sup> It is reasonable, therefore, that these properties can be further modified and exploited by mixing PbS nanocrystals with those of other semiconductors.<sup>31</sup>

This article presents a facile solution approach by which to synthesize  $\text{SnO}_2$ -PbS nanocomposites, using cetyl trimethyl ammonium bromide (CTAB) as a surface capping agent<sup>32</sup> and  $\text{Pb}(\text{NO}_3)_2$  and  $\text{Na}_2\text{S}\cdot 9\text{H}_2\text{O}$  as  $\text{Pb}^{2+}$  and  $\text{S}^{2-}$  sources, respectively (Fig. 1). The aim is to develop a synthetic route which utilizes (i) low temperatures, (ii) shorter reaction times, (iii) safe and inexpensive reagents and (iv) open vessels. This approach is in contrast to recent work aimed at producing nanomaterials for the photochemical passivation of dyes. Such work has, for example, yielded hybrid nanospheres<sup>33</sup> by extended and high temperature autoclave methods and by using expensive precious metal colloid. In other work, the synthesis of core@shell

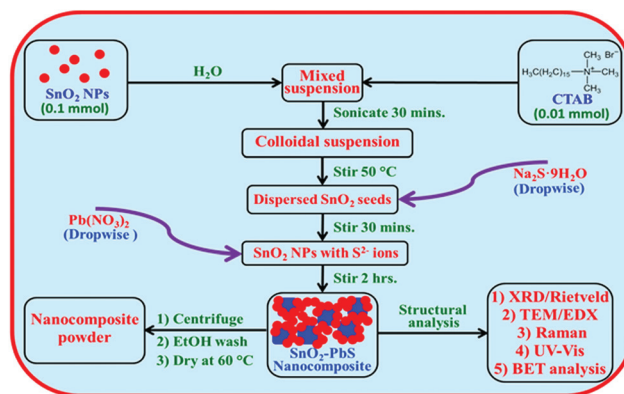


Fig. 1 Synthetic scheme for the preparation of  $\text{SnO}_2$ -PbS nanocomposites.

heterostructures *e.g.* of  $\text{SnO}_2$ @CdS has employed precious metal substrates and high temperatures whilst also necessitating the use of highly toxic precursors.<sup>23</sup> The structure, morphology and photocatalytic properties of new  $\text{SnO}_2$ -PbS nanocomposites are investigated and a model is developed based upon lattice relaxation processes manifest at the interfacial regions in the nanocomposites, which helps to explain how and why the two semiconductors interact.

## Experimental section

### Synthesis

**General synthetic and analytical details.** Chemicals were purchased from Sigma-Aldrich (reagents: analytical grade; solvents: HPLC grade) and used without further purification. Aqueous solutions were prepared using HPLC water (Millipore).

**$\text{SnO}_2$  nanoparticle preparation.**  $\text{SnCl}_4\cdot 5\text{H}_2\text{O}$  (0.351 g, 1.0 mmol) was dissolved in water (25 ml). CTAB (0.365 g, 1.0 mmol) was dissolved in water (5 ml) and added to the  $\text{SnCl}_4\cdot 5\text{H}_2\text{O}$  solution. The resulting mixture was stirred vigorously for 1 h until a clear solution was obtained. NaOH (0.8 g, 20.0 mmol) was dissolved in water (10 ml), and to this solution 10 ml of ethanol was added to make a basic mixture of alcohol and water (1 : 1). This was added dropwise to  $\text{SnCl}_4\cdot 5\text{H}_2\text{O}$  solution under continuous stirring. A white precipitate that had formed in the acidic reaction mixture dissolved once a pH of 11–12 was obtained. The solution was heated to reflux at 100 °C for 4 h. After cooling to room temperature, a white colloidal suspension of  $\text{SnO}_2$  nanoparticles (NPs) was obtained, which was centrifuged and the solid washed with water ( $\times 2$ ) and absolute ethanol ( $\times 3$ ) to remove impurities before being dried at 60 °C in air.

**$\text{SnO}_2$ -PbS nanocomposite preparation.** To make  $\text{SnO}_2$ -PbS nanocomposites, a soft chemical process (near ambient temperature reaction in an open vessel)<sup>34</sup> was used. In a typical process,  $\text{SnO}_2$  NPs<sup>35</sup> (0.015 g, 0.1 mmol) were dispersed in water (25 ml) by ultrasonication. CTAB (0.036 g, 0.1 mmol) was



added with vigorous stirring. The resulting dispersion was slowly elevated to 50 °C, retained at this temperature for 2 h and then allowed to cool to room temperature, after which flocculation was seen to have occurred. A 5 ml aqueous solution of Na<sub>2</sub>S·9H<sub>2</sub>O (0.024 g, 0.1 mmol) was added dropwise and the resulting mixture stirred for 30 min. Finally, a 5 ml aqueous solution of Pb(NO<sub>3</sub>)<sub>2</sub> (0.033 g, 0.1 mmol) was added dropwise to the system and the mixture stirred vigorously for another 2 h at room temperature. The SnO<sub>2</sub>-PbS nanocomposite was obtained by centrifugation and washed with water (2 × 25 ml) and absolute ethanol (3 × 25 ml) and then vacuum dried for 6 h to obtain the final product as a grey powder. See Fig. 1 above and for the synthesis of PbS nanocubes (NCs) undertaken using Na<sub>2</sub>S·9H<sub>2</sub>O with Pb(NO<sub>3</sub>)<sub>2</sub> in the absence of preformed SnO<sub>2</sub> NPs see ESI.†

### Nanomaterials characterization

**X-ray diffraction (XRD).** XRD profiles were recorded using Ni-filtered Cu K $\alpha$  radiation from a highly stabilized and automated PAN-analytical X-ray generator operated at 40 kV and 40 mA. The X-ray generator was coupled with a PW3071/60 Bracket goniometer for sample mounting. Step-scan data (step size 0.02° 2 $\theta$ , counting time 2 s per step) were recorded for 20°–75° 2 $\theta$ . Powder patterns were deconvoluted using the Rietveld whole-profile fitting method based on structure and microstructure refinement.<sup>36</sup> Rietveld software MAUD version 2.33<sup>37</sup> was used to carry out simultaneous refinement of both material structure and microstructure by a least squares refinement method. For the detailed procedure see ESI.†

**Transmission electron microscopy (TEM).** A Technai 20 high resolution (HR) TEM was used to scrutinize nanocrystal shape and size. Magnification 2.0.1 was used to count the diameters of 100 particles ( $N$ ), defining intervals of 0.25 nm between  $d_{\min} \leq d \leq d_{\max}$ . Size distributions were constructed with DataGraph 3.0 and morphology was analyzed using Digital Micrograph 3.6.5. Compositional analysis used a scanning transmission electron microscope (STEM, Technai Osiris). High-angle annular dark field (HAADF) imaging and energy-dispersive X-ray (EDX) spectrum imaging techniques were utilized to characterize individual structures. EDX spectrum image (SI) data was processed using machine learning methods implemented in HyperSpy.<sup>38</sup> In each case, analysis required sample preparation by droplet coating of ethanolic suspensions on carbon coated Au grids (Agar Scientific, 300 mesh).

**Raman spectroscopy.** Data were collected at room temperature on a Thermo Scientific DXR Raman microscope using a helium–neon laser with an excitation wavelength of 532 nm (laser power 10 mW).

**X-ray photoelectron spectroscopy (XPS).** XPS measurements were obtained using a Thermo Scientific K-Alpha system. The binding energy was calibrated internally based on the C 1s line position.

**Brunauer–Emmett–Teller (BET) surface area analysis.** BET surface areas of as-prepared samples were analyzed by nitrogen adsorption in a Tristar 3000 analyzer. Samples were degassed

at 77 K before nitrogen adsorption measurements were commenced. The BET surface areas were determined by a multi-point BET method using the adsorption data in the  $P/P_0$  range 0.0–1.0 (where  $P$  and  $P_0$  are the equilibrium and the saturation pressure of adsorbates at the temperature of adsorption).

**Photocatalytic experiments.** Photocatalytic activities of the as-prepared samples were evaluated by monitoring the degradation of RhB dye in water under simulated solar irradiation without sacrificial reagents at room temperature. In a typical process, 5.0 mg of catalyst was added to 40 ml of a  $1.0 \times 10^{-5}$  M aqueous solution of RhB (pH 7), and the mixture stirred in the dark for 2 h. to allow adsorption of the dye on the catalyst surface.<sup>39</sup> Thereafter, a 3.0 ml aliquot of the mixture was centrifuged and the absorption of the dye solution therein determined to obtain the dye concentration before photocatalysis ( $C_0$ ). The remaining solution was then irradiated with a 150 W xenon lamp fitted with an air mass 1.5 global (AM 1.5G) filter (Solar Simulator model LSO106, 1 sun illumination, 100 mW cm<sup>-2</sup>). Degradation of the RhB absorption maximum at 555 nm was monitored using a UV-vis spectrophotometer (Perkin Elmer LAMBDA 265) to obtain the concentration ( $C$ ) of dye as a function of time in subsequent aliquots. An ice cold water bath was used to prevent evaporation during catalysis and to avoid degradation due to heating. Two reference experiments, (i) without light irradiation in the presence of catalyst, and (ii) with light irradiation in the absence of catalyst were also undertaken and the degradation efficiency was calculated according to

$$\text{Degradation (\%)} = (1 - C/C_0) \times 100 \quad (1)$$

Apparent quantum yield ( $\phi_x$ ) was measured according to

$$\phi_x = \pm (d[x]/dt)/d[h\nu]_{\text{inc}}/dt \quad (2)$$

where  $d[x]/dt$  is the rate of change of the concentration of the reactant (or product) and  $d[h\nu]_{\text{inc}}/dt$  is the total optical power impinging on the sample.<sup>40</sup>

Hydroxyl radicals (OH $\cdot$ ) produced during photocatalysis were estimated by the fluorescence method using terephthalic acid (TA) as a probe molecule. In a typical process, a 5.0 mg portion of catalyst was dispersed in an aqueous solution of 30 ml of TA ( $5 \times 10^{-4}$  M) and NaOH ( $2 \times 10^{-3}$  M). The resulting suspension was exposed to simulated solar radiation and at regular intervals, 3.0 ml of the suspension was collected and centrifuged and the maximum fluorescence emission intensity measured with an excitation wavelength of 315 nm. This method relies on the fluorescence signal at 425 nm of 2-hydroxyterephthalic acid (TAOH).

## Results and discussion

### Phase identification by XRD

SnO<sub>2</sub> NPs and SnO<sub>2</sub>-PbS nanocomposites were prepared as described above. Fig. 2a shows the XRD pattern for SnO<sub>2</sub> NPs, with all peaks indexed with tetragonal SnO<sub>2</sub> phase (ICSD code 154960, space group  $P4_2/mnm$ ,  $a = b = 4.7331$  Å,  $c = 3.1815$  Å).



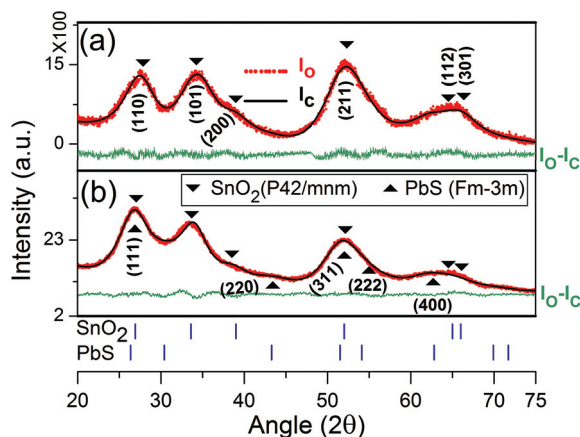


Fig. 2 Observed ( $I_O$ ) and simulated ( $I_C$ ) XRD patterns (indexed) of (a)  $\text{SnO}_2$  NPs and (b)  $\text{SnO}_2$ -PbS nanocomposites. The green lines represent  $I_O - I_C$ . Vertical markers corresponding to reflections from individual phases are shown in blue.

The breadth of the reflections indicates that the  $\text{SnO}_2$  NPs are relatively small.<sup>41</sup> (For the XRD pattern of PbS NCs see ESI Fig. S1.†) The XRD pattern of the  $\text{SnO}_2$ -PbS nanocomposites (Fig. 2b) is similar to that of the  $\text{SnO}_2$  NPs, the intensity ratio of the first two peaks (at low  $2\theta$ ) notwithstanding. In Fig. 2a the intensity ratio of these (110) and (101) reflections is essentially unity, but in Fig. 2b the (110) reflection appears more intense. This variation in the intensity ratio is attributed to the presence of peak overlap between PbS (111) and  $\text{SnO}_2$  (110). The same is true for  $\text{SnO}_2$  (211) and PbS (311). However, other reflections consistent with PbS are almost absent from the XRD pattern of  $\text{SnO}_2$ -PbS nanocomposites, indicating that the PbS component is rendered significantly amorphous by virtue

of its including a high degree of lattice imperfections. Resulting changes in microstructural parameters are summarized in Tables 1 and 2.

### Nanostructure evolution by X-ray diffraction

To interrogate micro/nano-structural defect parameters information related to, for example, signal full width at half-maximum (FWHM), intensity maxima, integrated intensity, and Gaussian content (Gaussianity)<sup>42</sup> was extracted using Rietveld analysis.<sup>43</sup> This method considers the isolated and overlapping reflections of all pertinent phases in a multiphase material and, in the present study, has been used to evaluate different structure/microstructure parameters in  $\text{SnO}_2$  NPs and  $\text{SnO}_2$ -PbS nanocomposites (Fig. 2). The Goodness-of-Fit value of each fitted pattern lies very close to unity. At  $a = 4.7764$  Å and  $c = 3.2558$  Å, the lattice parameters obtained for  $\text{SnO}_2$  NPs from the Rietveld refinement are slightly larger than the reported values (ICSD code 154960,  $a = 4.7331$  Å,  $c = 3.1815$  Å), suggesting an expansion of the unit cell volume from  $71.272$  Å<sup>3</sup> to  $74.277$  Å<sup>3</sup> as the particle size reduces to nanometer regime. Broadening of reflections results from the cumulative effect of both small particle size and r.m.s lattice strain, both of which are found to be anisotropic (Table 1).

The presence of cubic PbS phase alongside tetragonal  $\text{SnO}_2$  phase is clearly revealed by Fig. 3a, which highlights the significant intensity mismatches that result if the XRD pattern for  $\text{SnO}_2$ -PbS nanocomposites is fitted with only tetragonal  $\text{SnO}_2$  phase. Data indicate the presence of a small amount of PbS in the composite with very small particle size. The poor refinement quality in Fig. 3a significantly improves if the same XRD pattern is fitted with both  $\text{SnO}_2$  and PbS phases (Fig. 3b). Refinement suggests that the composite comprises a major  $\text{SnO}_2$  phase (~80 vol%) and a minor PbS phase (~20 vol%). The individual contribution of each of these phases along with the general background intensity in the XRD pattern is shown in Fig. 3c. Interestingly, and in contrast to either  $\text{SnO}_2$  or PbS, particle size and r.m.s lattice strain in the nanocomposites are isotropic in nature. In the nanocomposite, PbS is rather amorphous, resulting in the observation of very broad reflections centered around the most intense reflections of bulk PbS which coincide with the nanocrystalline  $\text{SnO}_2$  reflections. The nature of the PbS component of the nanocomposite explains the lack of strong crystalline reflections attributable to PbS in the XRD pattern. It is also evident in Table 2 that the particle size of this PbS has been significantly reduced relative to that seen for pure PbS. Moreover, the highly distorted cubic phase

Table 1 Microstructural parameters obtained for  $\text{SnO}_2$  NPs

Lattice parameters (Å)		Anisotropic particle size (nm)	Direction (plane)	Anisotropic lattice strain
$a$	$c$			
4.7764	3.2558	2.11	110	0.0058
		4.59	101	0.0408
		2.39	200	0.0783
		3.40	211	0.0248
		3.12	112	0.0482
		4.74	301	0.0182

Table 2 Microstructural parameters obtained for  $\text{SnO}_2$ -PbS nanocomposites

Phase	Vol. fraction	Lattice parameters (Å)		Particle size (nm)	Strain	Fractional coordinate of oxygen	
		$a$	$c$			$x$	$y$
$\text{SnO}_2$ ( $P4_2/mnm$ )	79.88	4.7845	3.2247	2.89	0.020	0.3465	0.1845
PbS ( $Fm\bar{3}m$ )	20.12	5.9746		2.60	0.041		





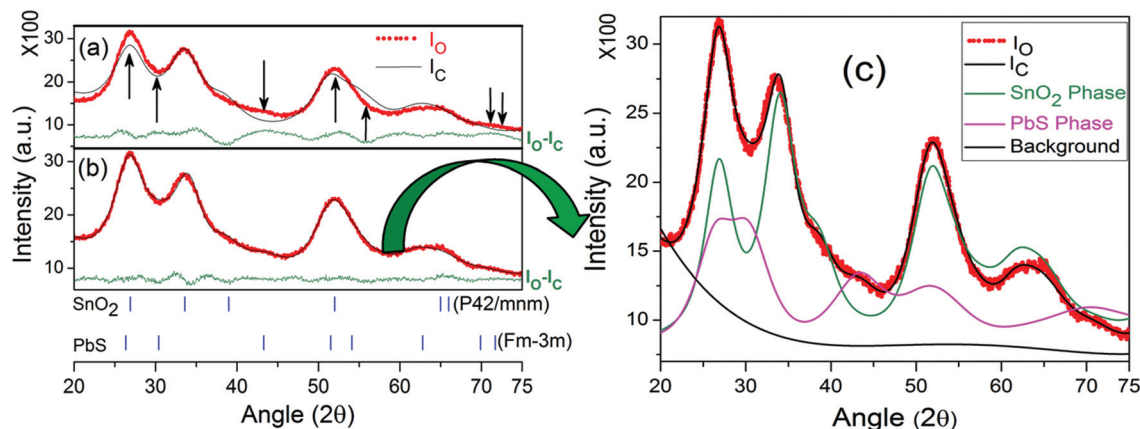


Fig. 3 Typical Rietveld refinement output pattern for SnO<sub>2</sub>-PbS nanocomposites employing (a) tetragonal SnO<sub>2</sub> phase only and (b) both tetragonal SnO<sub>2</sub> and cubic PbS phase. (c) The contribution of tetragonal SnO<sub>2</sub>, cubic PbS and background to the XRD pattern for SnO<sub>2</sub>-PbS nanocomposites.

with the extended  $a$  value demonstrates approximately four times as much lattice strain as nanocrystalline PbS (Table S1†).

To understand the changes associated with different microstructural parameters in the atomic arrangements in SnO<sub>2</sub> NPs, PbS NCs and SnO<sub>2</sub>-PbS nanocomposites atomic models of tetragonal SnO<sub>2</sub> (Fig. S3), cubic PbS (Fig. S4) and SnO<sub>2</sub>-PbS nanocomposites (Fig. S5) have been designed and are analyzed critically in the ESI.†

### TEM analysis

TEM and HRTEM images and fast Fourier transform (FFT) patterns of SnO<sub>2</sub> NPs are given in Fig. 4 and S6.† Fig. 4 demonstrates the presence of NPs of mean size of  $4.2 \pm 1.0$  nm; the measured fringe spacing being 0.33 nm, suggesting the (110) plane of tetragonal SnO<sub>2</sub>.<sup>16</sup> (For representative TEM images and an FFT pattern of PbS NCs see ESI Fig. S7 and S8.†)

Preliminary TEM images of SnO<sub>2</sub>-PbS nanocomposites suggest the formation of a composite structure (see Fig. S9†).

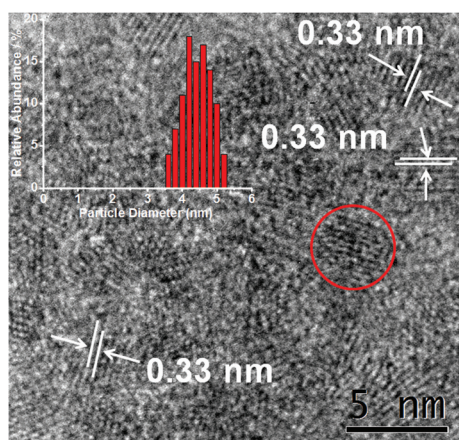


Fig. 4 A representative HRTEM image of SnO<sub>2</sub> NPs indicating measured distances between the lattice planes and the particle size distribution for the sample (top left). The area in the red circle was subjected to FFT (see ESI Fig. S6b†).

To further elucidate this STEM-HAADF imaging and EDX spectrum imaging techniques were employed. The separation of component signals using independent component analysis (ICA) allows for reconstruction of the heterogeneous nanocomposite using a method which, unlike in conventional EDX mapping, is free of external bias, except for the choice of the number of components. ICA, implemented in HyperSpy,<sup>38</sup> was carried out on an EDX spectrum image (unprocessed EDX data is shown in ESI Fig. S10 and S11†). The multi-dimensional dataset was reduced and projected onto five maximally independent dimensions labeled IC#0 to IC#4 in Fig. 5 (see also ESI†). IC#0 contains both Cu-K $\alpha$  and Au-L $\alpha$  and -M $\alpha$  peaks, which likely originate from secondary scattering by Cu in the sample holder and Au in the support grid, respectively. IC#1 contains Pb-L, Pb-M, Cu-K $\alpha$  and S-K $\alpha$  X-ray lines. Ignoring the Cu-K $\alpha$  peak, the pairing of Pb and S X-ray lines in the component spectrum is strong evidence that the X-rays originate from a Pb-S compound.<sup>44</sup> IC#2 contains Sn-K, Sn-L, Cu-K $\alpha$ , Si-K $\alpha$  and N-K $\alpha$  peaks (the last two we attribute to minor contamination). It is expected that if a SnO<sub>2</sub> compound is present then both Sn and O peaks should be captured in a single component, as was the case for IC#1. However, the very low energy oxygen peak suffers from strong attenuation in the sample on the path to the detector, causing variability in the signal strength of O relative to Sn as a function of location. This may explain why ICA has isolated oxygen as a single component (IC#4). Finally, IC#3 contains only a C-K $\alpha$  peak, and it is mapped to the location of the amorphous holey carbon support film as expected.

### Raman spectroscopy

Raman spectroscopy was applied to the structural characterization of the SnO<sub>2</sub> NPs and SnO<sub>2</sub>-PbS nanocomposites. The SnO<sub>2</sub> NPs are rutile in nature and occupy the space group  $P4_2/mnm$  ( $D_{4h}$ ), having the Raman active modes  $B_{1g}$ ,  $E_g$ ,  $A_{1g}$ , and  $B_{2g}$ . Fig. 6a shows the spectrum of SnO<sub>2</sub> NPs at room temperature, revealing peaks at  $484\text{ cm}^{-1}$ ,  $571\text{ cm}^{-1}$  and  $762\text{ cm}^{-1}$ . Those at  $484\text{ cm}^{-1}$  and  $762\text{ cm}^{-1}$  are consistent with rutile



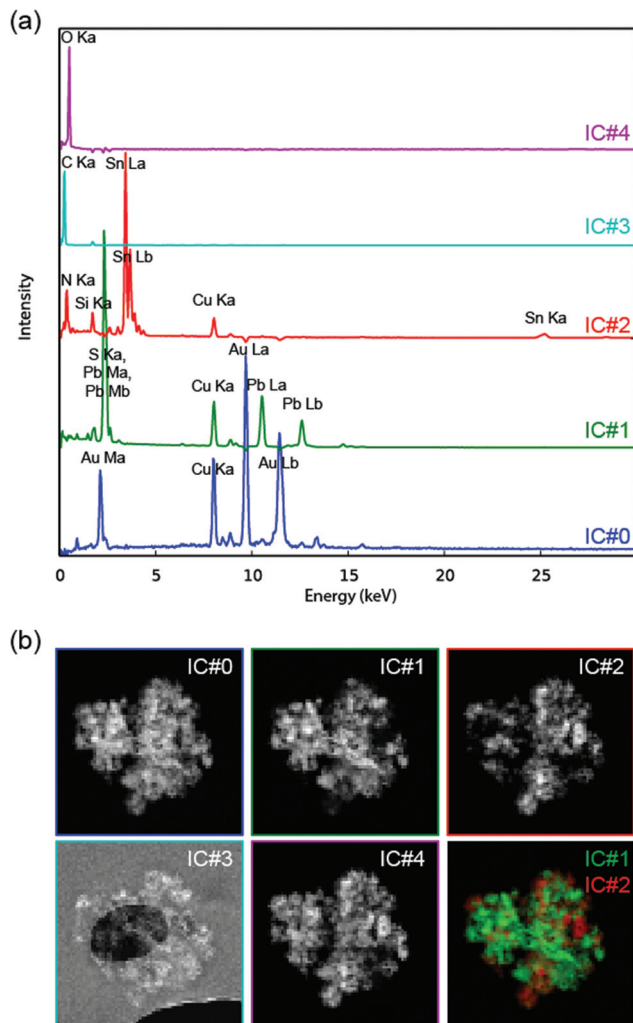


**Fig. 5** ICA results obtained from an EDX spectrum image of a  $\text{SnO}_2$ -PbS nanocomposite structure. (a) Independent component spectra containing the X-ray lines for the elements present (Au and Cu attributable to grid and sample holder). Independent component maps (b) IC#0-#4 are interspersed throughout the region. IC#1 represents a Pb rich phase, IC#2 a Sn rich phase, and IC#3 the carbon supporting film. Bottom right is an artificially coloured overlay of the IC#1 (green) and IC#2 (red) maps.

bulk  $\text{SnO}_2$ <sup>45</sup> and that at  $571\text{ cm}^{-1}$  is attributable to a  $\text{SnO}_2$  nanocrystal surface defect.<sup>46</sup> Broadening of the  $\text{B}_{2g}$  peak in comparison to that of bulk  $\text{SnO}_2$  is also characteristic of the nanocrystalline nature of the sample.<sup>45</sup> Moreover, the relative contribution of the defect-related peak at  $571\text{ cm}^{-1}$  (mostly due to surface oxygen vacancies)<sup>47</sup> is large compared to the main Raman active modes for  $\text{SnO}_2$  by virtue of the large surface area of the small  $\text{SnO}_2$  NPs. Fig. 6b shows the Raman spectrum of  $\text{SnO}_2$ -PbS nanocomposites. The strong peak at  $630\text{ cm}^{-1}$  is assigned to  $\text{SnO}_2$  NPs,<sup>26</sup> whereas peaks at  $486\text{ cm}^{-1}$  and  $768\text{ cm}^{-1}$  are consistent with rutile bulk  $\text{SnO}_2$ .<sup>45</sup> The existence of PbS in the nanocomposite is indicated by the strong peak at  $972\text{ cm}^{-1}$  (for Raman data on PbS NCs at room temperature see ESI Fig. S12†).<sup>48</sup> Moreover, the peak in Fig. 6a

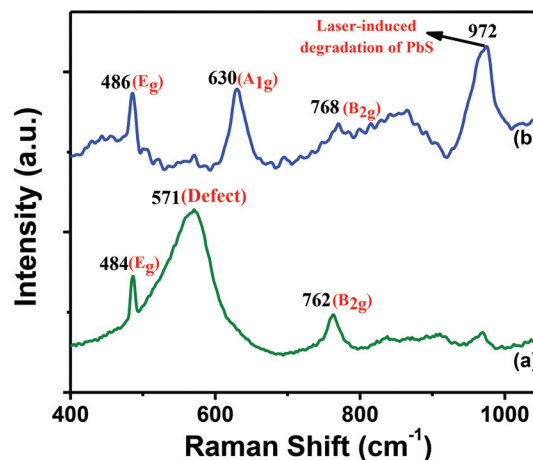


**Fig. 6** Raman spectra of (a)  $\text{SnO}_2$  NPs and (b)  $\text{SnO}_2$ -PbS nanocomposites.

attributed to a  $\text{SnO}_2$  nanocrystal surface defect mode is translated to the spectrum of the nanocomposite at  $630\text{ cm}^{-1}$ , indicating that  $\text{SnO}_2$  nanocrystallite surfaces are modified by the inclusion of PbS.

### XPS analysis

ESI Fig. S13 and S14† show XPS data that confirm the Sn oxidation state as (iv)<sup>49</sup> and the identity of the  $\text{SnO}_2$  NPs,<sup>50</sup> while Fig. S15 and S16† confirm PbS.<sup>51</sup> However, the peaks at  $136.7\text{ eV}$  and  $141.6\text{ eV}$  in Fig. S16a† (attributable to  $\text{Pb } 4f_{7/2}$  and  $\text{Pb } 4f_{5/2}$ , respectively<sup>52</sup>) each exhibit a shoulder (at  $137.5\text{ eV}$  and  $142.2\text{ eV}$ , respectively) that points to a close relationship between Pb and O (see below).<sup>53</sup> Moreover, the S  $2p$  region shows signals ( $159.9$  and  $161.0\text{ eV}$ ) attributable to  $\text{S } 2p_{3/2}$  and  $\text{S } 2p_{1/2}$ <sup>54</sup> alongside a peak at  $167.6\text{ eV}$  which indicates the formation of some  $\text{S(vi)}$  (Fig. S16b†).<sup>55</sup>

XPS analysis of the  $\text{SnO}_2$ -PbS nanocomposite is shown in Fig. 7 (for the survey spectrum see ESI Fig. S17†). Fig. 7a shows the Sn  $3d$  region and reveals symmetric signals attributable to  $\text{Sn(IV) Sn } 3d_{5/2}$  and  $\text{Sn } 3d_{3/2}$  binding energies.<sup>56</sup> The O  $1s$  peak is observed at  $530.0\text{ eV}$  (Fig. 7b). The peaks at  $138.0\text{ eV}$  and  $142.8\text{ eV}$  belong to the binding energy of  $\text{Pb } 4f_{7/2}$  and  $\text{Pb } 4f_{5/2}$ , respectively (Fig. 7c),<sup>52</sup> whilst S  $2p$  is characterized by peaks at  $160.4\text{ eV}$  (ref. 51) and  $167.6\text{ eV}$  (Fig. 7d).<sup>57</sup> An increase in binding energy can be seen for the Sn  $3d_{5/2}$ , Sn  $3d_{3/2}$  and O  $1s$  peaks as well as for the  $\text{Pb } 4f_{7/2}$ ,  $\text{Pb } 4f_{5/2}$  and S  $2p$  peaks in the nanocomposite relative to the analogous peaks for pure  $\text{SnO}_2$  and pure PbS. This suggests electronic interaction between  $\text{SnO}_2$  and PbS components,<sup>58</sup> with similar peak shifting having been observed previously for  $\text{SnO}_2$ - $\text{In}_2\text{O}_3$  nanocomposites.<sup>22</sup> Significantly, the  $\text{Pb } 4f_{7/2}$  and  $\text{Pb } 4f_{5/2}$  peaks in the nanocomposite have completely migrated to the positions occupied by the high-energy shoulders in PbS (see above, viz. Fig. S16a† and Fig. 7c); this suggests a greater intimacy between Pb and electronegative O in the nanocomposite.



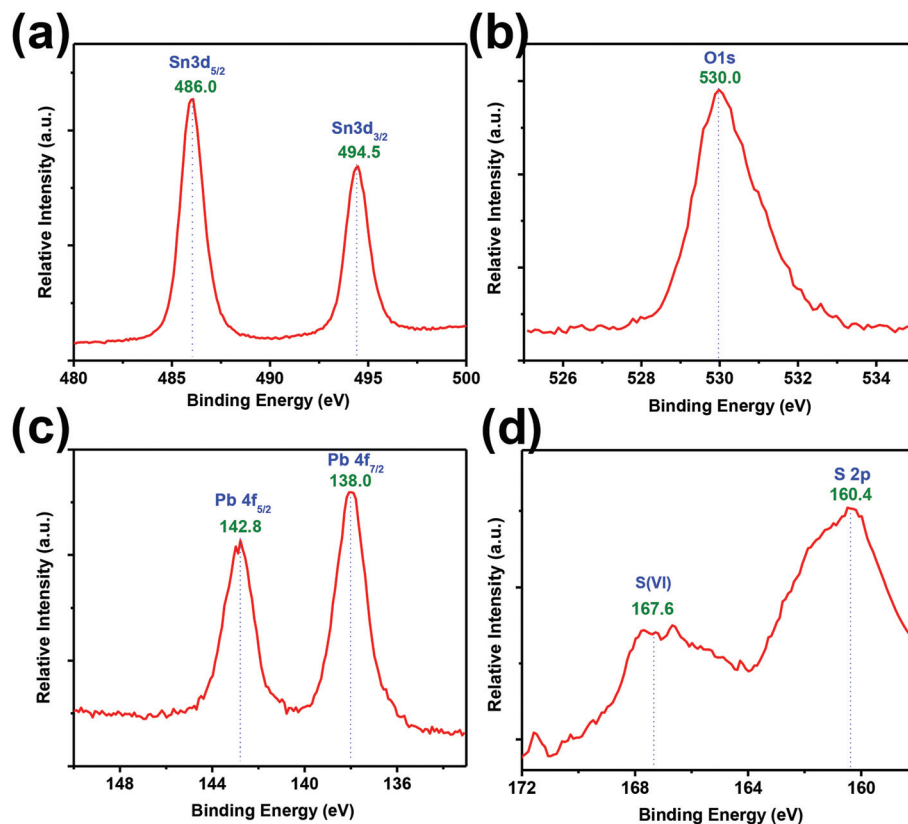


Fig. 7 XPS data for  $\text{SnO}_2$ -PbS nanocomposites: binding energy spectra for Sn 3d (a), O 1s (b), Pb 4f (c), and S 2p (d).

### UV-Vis spectroscopy

The UV-Visible absorption spectrum for an ethanolic solution of  $\text{SnO}_2$ -PbS nanocomposites is illustrated in Fig. 8 (for those of  $\text{SnO}_2$  and PbS see Fig. S18<sup>†</sup>). The UV-Vis absorption spectrum reveals two prominent absorption bands. That at 222 nm is assigned to the absorption of the  $\text{SnO}_2$  component<sup>59</sup> whilst

that at 270 nm can be attributed to the characteristic absorption of the PbS component.<sup>60</sup> The absorption edges for both  $\text{SnO}_2$  and PbS components in the  $\text{SnO}_2$ -PbS nanocomposites are slightly blue shifted relative to their analogues in the spectra of  $\text{SnO}_2$  and PbS nanocrystals, and this indicates that the sizes of  $\text{SnO}_2$  and PbS regions in the nanocomposites are modified in comparison to the corresponding sizes of pure  $\text{SnO}_2$  or PbS.<sup>61</sup> In this vein, related blue shifts of  $\lambda_{\text{max}}$  values in nanocomposite materials in comparison to those of their individual components have been documented previously.<sup>62</sup>

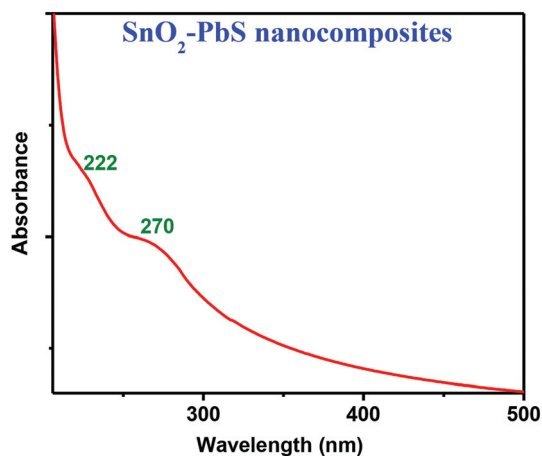


Fig. 8 UV-Vis absorption spectrum of  $\text{SnO}_2$ -PbS nanocomposites in aqueous solution.

### Photocatalytic degradation of Rhodamine B

The abilities of  $\text{SnO}_2$  NPs and  $\text{SnO}_2$ -PbS nanocomposites to photodegrade Rhodamine B (RhB) dye in aqueous solution under simulated solar irradiation have been studied. In each photocatalytic experiment, 5.0 mg of catalyst was used along with 40 mL of  $1.0 \times 10^{-5}$  M aqueous solution of RhB. The outcomes of tests are given in Fig. 9 and show the relationship between light absorbance at  $\lambda_{\text{max}} = 555$  nm and irradiation time for the dye. The major absorption band steadily reduced with increased irradiation time in both cases, though the rate of decrease proved significantly dissimilar for each sample. Two reference experiments (i) without light irradiation in the presence of the catalyst ( $\text{SnO}_2$ -PbS nanocomposite), and (ii) with light irradiation in the absence of catalyst were also





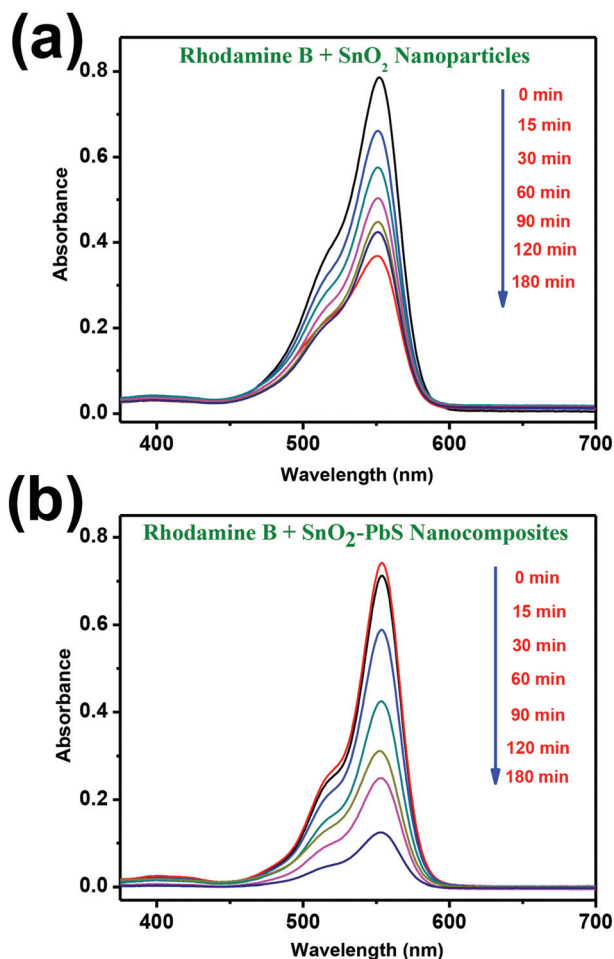


Fig. 9 Photolytically-induced spectral changes to the RhB (40 mL of  $1.0 \times 10^{-5}$  M aqueous solution) absorption maximum at ca. 555 nm on treatment with  $\text{SnO}_2$  NPs (a) and  $\text{SnO}_2$ -PbS nanocomposites (b) (5.0 mg of catalyst in each case).

performed. Neither of these experiments showed significant degradation of the dye (see ESI Fig. S19†).

Fig. 10a illustrates the decomposition rate for RhB  $\lambda_{\text{max}}$  as a function of irradiation time under identical conditions.  $C_0$  and  $C$  are the concentrations of RhB before and after irradiation, respectively. Notably, 84% of the dye was degraded by the presence of  $\text{SnO}_2$ -PbS nanocomposites after 180 min. irradiation, whilst only 53% degradation was observed for the use of pure  $\text{SnO}_2$  NPs (for data obtained using PbS see ESI Fig. S20†). Though enhancements comparable to that seen using  $\text{SnO}_2$ -PbS nanocomposites have been reported previously, it is noteworthy that prior work necessitated the use of precious metals and demanding synthetic conditions. For example, similar photocatalysis has been noted using Au- $\text{SnO}_2$  hybrid nanostructures prepared employing an autoclave at 200 °C for 12 h.<sup>33</sup> In a similar vein,  $\text{SnO}_2$ -CdS heterostructures proved highly active but necessitated the use of Au-based precursors and temperatures >800 °C as well as highly toxic Cd(II) reagents.<sup>23</sup> In contrast the current work deploys Sn/Pb reagents at <50 °C over 3–4 h.

To quantitatively compare the photocatalytic activities of these samples, the reaction rate constants ( $k$ ) were calculated by adopting the pseudo first-order model (eqn (3)) typically used to describe photocatalytic degradation assuming a low initial concentration of pollutant.<sup>63</sup>

$$\ln(C_0/C) = kt \quad (3)$$

Plots of  $\ln(C_0/C)$  versus irradiation time ( $t$ ) are provided in Fig. 10b, the linear relationships pointing to each photodegradation following first order kinetics. Apparent rate constants were determined to be  $3.3 \times 10^{-3}$  and  $10.5 \times 10^{-3} \text{ min}^{-1}$  for  $\text{SnO}_2$  NPs and  $\text{SnO}_2$ -PbS nanocomposites, respectively, demonstrating the photocatalytic activity of the  $\text{SnO}_2$ -PbS nanocomposites to be about 3 times higher than that of  $\text{SnO}_2$  NPs.

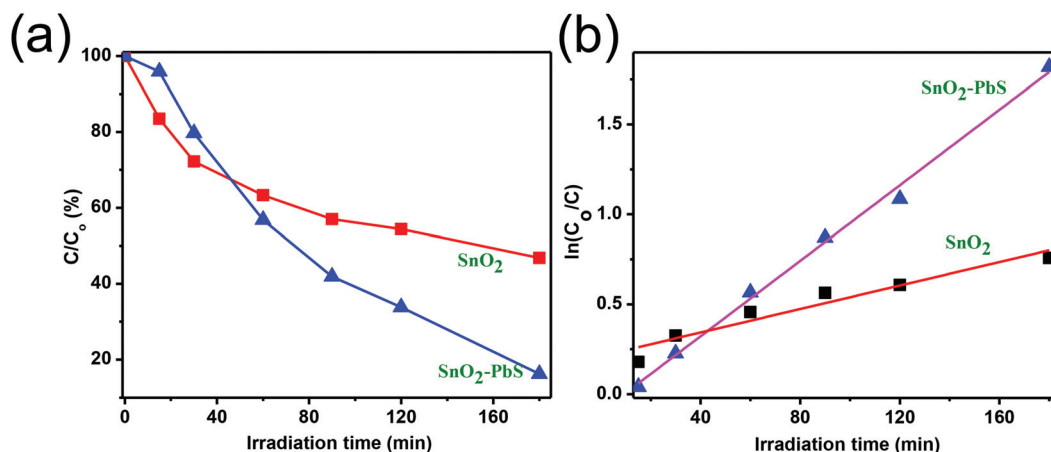


Fig. 10 (a) Plot of  $C/C_0$  (%) (where  $C_0$  and  $C$  are the concentrations of dye before and after irradiation, respectively) for RhB as a function of irradiation time in the presence of  $\text{SnO}_2$  NPs and  $\text{SnO}_2$ -PbS nanocomposites. (b) Plot of  $\ln(C_0/C)$  as a function of irradiation time.





### Catalyst recyclability and stability

To check the stability and reusability of the SnO<sub>2</sub>-PbS nanocomposite, cycling experiments on the photodegradation of RhB were undertaken with the catalyst recovered by centrifugation between tests. As illustrated in Fig. 11a, after three cycles of RhB photodegradation, the activity of SnO<sub>2</sub>-PbS nanocomposite revealed little loss of activity; the degradation efficiency of SnO<sub>2</sub>-PbS nanocomposite wrt RhB after the first, second, and third cycles being 84, 80, and 74%, respectively. The slightly reduced effectiveness of the catalyst in the third cycle can be tentatively attributed to photobleaching of the surface.<sup>64</sup> Nevertheless, these data suggest SnO<sub>2</sub>-PbS nanocomposite to be stable and to avoid significant deactivation during RhB photodegradation. In addition to photocatalytic activity, the stability of photocatalysts is highly relevant to applications development and the crystalline structure of the SnO<sub>2</sub>-PbS nanocomposite has been investigated after photodegradation experiments. Fig. 11b illustrates the XRD patterns of photocatalysts before and after three RhB

decomposition cycles, with the lack of observable changes indicating that both crystalline phase and structure remain intact.

### Product analysis and reaction mechanism

It is recognized that hydroxyl radicals produced by the illumination of photocatalysts represent the key active species in degrading organic molecules. Consistent with the thermodynamic obligation for creating OH<sup>•</sup>, the valence band (VB) and the conduction band (CB) of the semiconductor photocatalyst should be positioned such that the oxidation potential of the hydroxyl radical ( $E_{\text{H}_2\text{O}/\text{OH}^\bullet}^\circ = 2.8 \text{ V vs. normal hydrogen electrode (NHE)}$ ) and the reduction potential of superoxide radicals ( $E_{\text{O}_2/\text{O}_2^{\bullet-}}^\circ = -0.28 \text{ V vs. NHE}$ ) lie well within the band gap of the photocatalyst.<sup>65</sup> The relative band positions of the two semiconductors were examined, as the band-edge potential plays a critical role in determining the transport of photoexcited charge carriers at a heterojunction. The low energy limits of the conduction band ( $E_{\text{CB}}$ ) of each component were estimated empirically according to<sup>66</sup>

$$E_{\text{CB}/\text{VB}} = X - 0.5E_g + E_0 \quad (4)$$

where  $E_g$  is the band gap energy of the semiconductor,  $E_0$  is the scale factor relating the reference electrode redox level to the absolute vacuum scale ( $E_0 = -4.5 \text{ eV}$  for NHE), and  $X$  is the electronegativity of the semiconductor, which can be expressed as the geometric mean of the absolute electronegativities of the constituent atoms. The  $X$  values for SnO<sub>2</sub> and PbS are 2.59 and 2.19 eV, respectively, and the band gap energies of SnO<sub>2</sub> and PbS are 3.61 and 0.41 eV, respectively. Following eqn (4) the  $E_{\text{CB}}$  values of SnO<sub>2</sub> and PbS become  $-3.72$  and  $-2.52 \text{ eV}$ , respectively. Likewise, the high energy limit of the valence bands ( $E_{\text{VB}}$ ) of SnO<sub>2</sub> and PbS become  $-7.33$  and  $-2.93 \text{ eV}$ , respectively. This makes both the  $E_{\text{CB}}$  and the  $E_{\text{VB}}$  of PbS higher than their counterparts in SnO<sub>2</sub>. The bottom of the CB and the top of the VB of SnO<sub>2</sub> lie at  $-0.78$  and  $2.83 \text{ eV}$  with respect to NHE, whilst the corresponding values for PbS are  $-1.98$  and  $-1.57 \text{ eV}$ , meaning that neither SnO<sub>2</sub> nor PbS can independently accomplish the thermodynamic prerequisite for OH<sup>•</sup> generation. Taking into account the band gap,  $E_{\text{CB}}$  and  $E_{\text{VB}}$  in PbS and SnO<sub>2</sub> it follows that the band disposition of the SnO<sub>2</sub>-PbS nanocomposite promotes the separation and transportation of photoinduced charge carriers, leading to elevated photocatalytic activity. Fig. 12 shows how the type-II configuration of the nanocomposite diminishes the electron-hole recombination probability, allows one to boost electron mobility, and separates charge carriers; under irradiation, photo-generated electrons in PbS move to the SnO<sub>2</sub>, while the photogenerated holes are left in the valence band of PbS. Electron acceptors such as adsorbed O<sub>2</sub> can trap electrons at the SnO<sub>2</sub> surface to produce superoxide radical anions (O<sub>2</sub><sup>•-</sup>), which undergo protonation to yield hydroperoxy radicals (HO<sub>2</sub><sup>•</sup>). In water, these then yield strongly oxidizing hydroxyl radicals (OH<sup>•</sup>), which efficiently decompose organic pollutants like RhB. Lastly, photoinduced holes in PbS can

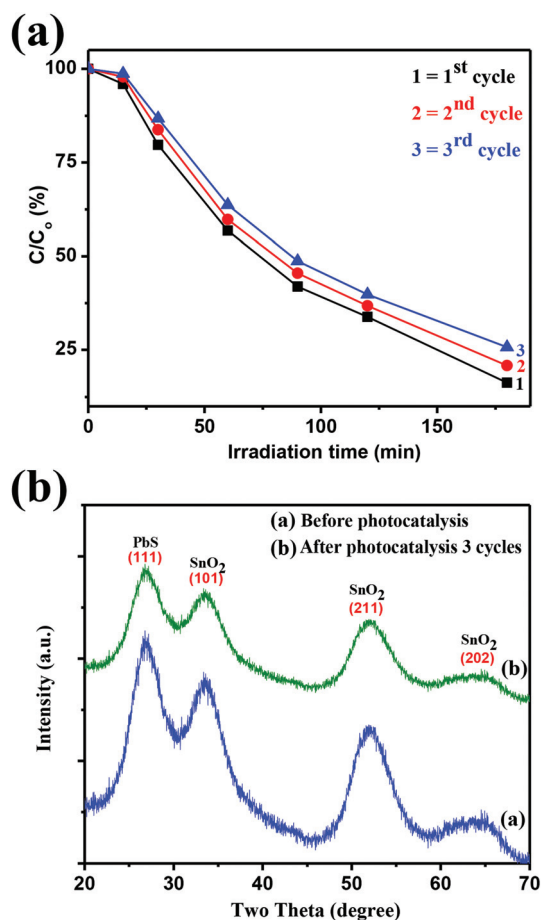


Fig. 11 (a) Reproducibility of the photocatalytic decomposition of RhB using fresh (cycle 1) and recycled (cycles 2 and 3) SnO<sub>2</sub>-PbS and (b) XRD patterns of SnO<sub>2</sub>-PbS nanocomposite before and after these tests.



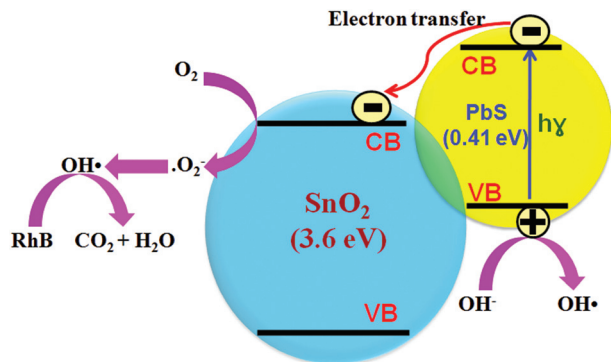
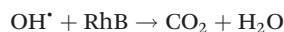
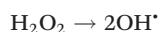
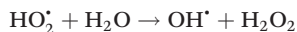
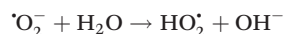
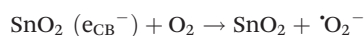
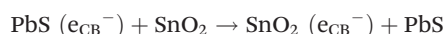


Fig. 12 Model for the high photocatalytic activity and stability of SnO<sub>2</sub>-PbS nanocomposites.

also be trapped by OH<sup>-</sup>, so acting as another source of OH<sup>·</sup>. Overall, the mechanism for the photocatalytic degradation of RhB can be expressed as:



To verify that photocatalytic degradation in the current system proceeds through photoinduced OH<sup>·</sup> radical formation a terephthalic acid (TA) probe was used, whereby reaction of TA with OH<sup>·</sup> radicals to generate fluorescent 2-hydroxy-terephthalic acid (TAOH) was monitored.<sup>67</sup> Upon excitation at 315 nm, the maximum intensity at 425 nm was determined to steadily increase with irradiation time (Fig. 13), indicating the photogeneration of OH<sup>·</sup>. (Fig. S21† illustrates the linear increase in  $\lambda_{\text{max}} = 425$  nm with irradiation time.) Importantly, and in line with previous reports,<sup>67,68</sup> the TA probe substantiates the photocatalytic mechanism proposed above, requiring the presence of a type-II system to explain radical formation.

### Measurement of apparent quantum yield

The apparent quantum yield ( $\phi_x$ ) of the SnO<sub>2</sub>-PbS nanocomposite with respect to aqueous RhB was determined using a 150 W xenon lamp fitted with an AM 1.5G filter ( $I = 100$  mW

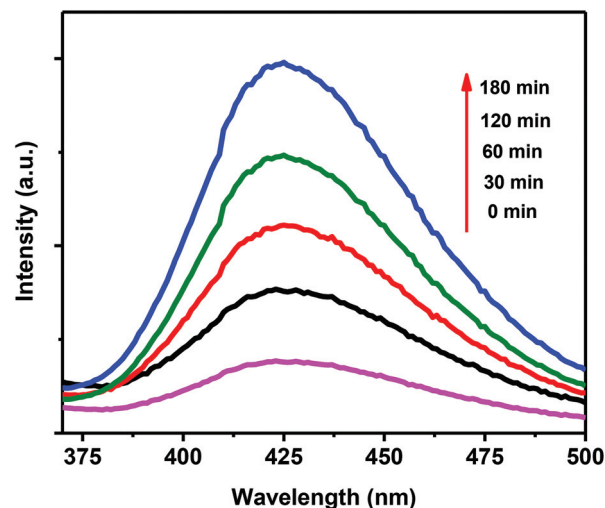


Fig. 13 Fluorescence spectral changes measured during illumination of SnO<sub>2</sub>-PbS nanocomposite in a basic solution of TA (excitation at 315 nm).

cm<sup>-2</sup>). We calculated  $\phi_x$  to be 0.217 mol min<sup>-1</sup> W<sup>-1</sup> using 5.0 mg catalyst in 40 mL of a  $1.0 \times 10^{-5}$  M aqueous solution of RhB at pH 7. In recycling tests (see above)  $\phi_x$  values obtained for the 2<sup>nd</sup> and 3<sup>rd</sup> cycles were 0.214 and 0.208 mol min<sup>-1</sup> W<sup>-1</sup>, respectively.

### Comparison of photocatalytic activity with P25

The performance of the SnO<sub>2</sub>-PbS nanocomposite has been compared with that of the standard TiO<sub>2</sub> Degussa P25 powder (P25).<sup>69</sup> Results shown in Fig. S22† establish that P25 (5.0 mg) induces a steady decrease in the 555 nm absorption band of RhB with an efficiency which, at 70%, is low compared to that displayed by the new SnO<sub>2</sub>-PbS nanocomposite photocatalyst (84%) (Fig. 14).

### BET surface area analysis

The importance of surface area to heterogeneous photocatalysis derives from the ability of a larger surface area to furnish more active sites for the adsorption of reagent molecules.<sup>70</sup> In this work, BET surface areas and pore size distributions were determined for SnO<sub>2</sub> NPs and SnO<sub>2</sub>-PbS nanocomposites by measuring nitrogen adsorption-desorption isotherms (Fig. S23†). Both the adsorption and desorption branches of each of the recorded isotherms were found to be similar, meaning that they displayed type IV behaviour and distinct H2-type hysteresis loops.<sup>71</sup> This suggests that either sample incorporates an interconnected network of mesopores<sup>63</sup> with a disordered and inhomogeneous distribution of sizes<sup>72</sup> characteristic of mesoporous structure formation through the aggregation of primary crystallites.<sup>73</sup> Specific BET surface areas and pore volumes and sizes are summarized in Table 3. Notably, and in a similar vein to previous reports,<sup>74,75</sup> the



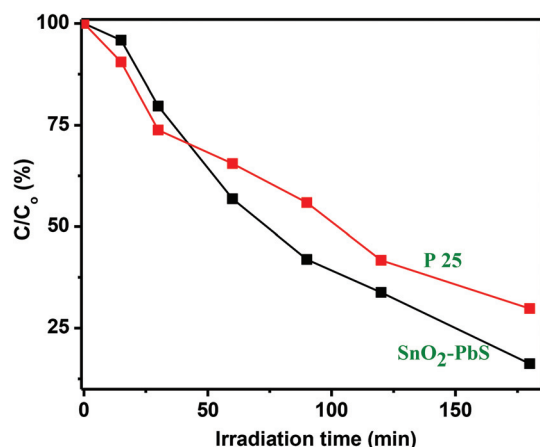


**Fig. 14** A comparison of  $C/C_0$  (%) as a function of irradiation time for RhB solutions treated with  $\text{SnO}_2$ -PbS nanocomposite and P25 (5.0 mg in either sample).

**Table 3** Nitrogen sorption porosimetry studies<sup>a</sup> of as-synthesized  $\text{SnO}_2$  NPs and  $\text{SnO}_2$ -PbS nanocomposites

Photocatalyst	$S_{\text{BET}}$ ( $\text{m}^2 \text{g}^{-1}$ )	Pore volume ( $\text{cm}^3 \text{g}^{-1}$ )	Mean pore size (nm)
$\text{SnO}_2$	128.0795	0.138662	3.8260
$\text{SnO}_2$ -PbS	107.1704	0.207755	6.6975

<sup>a</sup> Surface areas determined by the BET technique, mean pore diameters by BJH theory (applied to the adsorption branch), and pore volumes by single-point analysis.

surface area of pure  $\text{SnO}_2$  NPs ( $128.0795 \text{ m}^2 \text{g}^{-1}$ ) exceeds that recorded for the  $\text{SnO}_2$ -PbS nanocomposite ( $107.1704 \text{ m}^2 \text{g}^{-1}$ ), arguing against a simple correlation between surface area and photocatalytic activity.<sup>69</sup> Taken together with the use of a TA probe to monitor photoinduced  $\text{OH}^\bullet$  radical formation, these results support a type-II interaction in the  $\text{SnO}_2$ -PbS nanocomposite leading to the enhancement of photocatalytic activity.

## Conclusions

In summary, we have developed a facile and cost-effective approach to the synthesis of a  $\text{SnO}_2$ -PbS nanocomposite, the nature of which has been comprehensively elucidated. Significantly, compared to pure  $\text{SnO}_2$ , the  $\text{SnO}_2$ -PbS nanocomposite displays enhanced photocatalytic activity and good structural stability for RhB degradation under simulated solar irradiation. An apparent quantum yield of  $0.217 \text{ mol min}^{-1} \text{W}^{-1}$  is calculated for the  $\text{SnO}_2$ -PbS nanocomposite system and good recyclability is established. The composite structure is considered to improve the separation of photogenerated electron-hole pairs, thus enhancing the photocatalytic response. It is anticipated that this  $\text{SnO}_2$ -PbS nanocomposite may provide a new approach to high performance, novel catalyst

design and fabrication targeting new energy sources, green chemistry solutions, and addressing environmental issues. The facile synthetic method used is now being extended to other tin-containing nanocomposites, with efforts also being directed towards ensuring optimal recyclability, with an overall view to the design and cost-effective synthesis of advanced nanomaterials with specific properties for functional applications.

## Acknowledgements

A. K. and D. R. acknowledge support from the Royal Society's Newton International Fellowship scheme. D. R. would also like to thank Prof. Paul Midgley for access to the TEM at the University of Cambridge and Prof. Gianluigi Botton for access to the CCEM, a national facility supported by NSERC, the Canada Foundation for Innovation and McMaster University. B. R. K. thanks the UK EPSRC for financial support (EP/J500380/1). Thanks go also to Drs Tim Jones and Jill Geddes of Schlumberger Gould Research for help with the acquisition of Raman and X-ray photoelectron spectra and to Dr Zlatko Saracevic of the Department of Chemical Engineering and Biotechnology (University of Cambridge) for help with BET surface area analysis. The authors would also like to thank Miss Georgina Hutton (University of Cambridge) for valuable discussions and input. Unprocessed data for this paper are available at the University of Cambridge data repository (see <https://www.repository.cam.ac.uk/handle/1810/252973>). These include some data in the file format .dm3 (HRTEM data), which can be opened using the software program Gatan Digital Micrograph 3.6.5 or similar.

## References

- 1 R. Roy, R. A. Roy and D. M. Roy, *Mater. Lett.*, 1986, **4**, 323–328.
- 2 V. L. Colvin, M. C. Schlamp and A. P. Alivisatos, *Nature*, 1994, **370**, 354–357; B. O. Dabbousi, M. G. Bawendi, O. Onitsuka and M. F. Rubner, *Appl. Phys. Lett.*, 1995, **66**, 1316–1318.
- 3 C. Lu, C. Guan, Y. Liu, Y. Cheng and B. Yang, *Chem. Mater.*, 2005, **17**, 2448–2454; X. Lu, Y. Zhao and C. Wang, *Adv. Mater.*, 2005, **17**, 2485–2488.
- 4 V. Salgueiriño-Maceira and M. A. Correa-Duarte, *Adv. Mater.*, 2007, **19**, 4131–4144; B. Y. S. Kim, W. Jiang, J. Oreopoulos, C. M. Yip, J. T. Rutka and W. C. W. Chan, *Nano Lett.*, 2008, **8**, 3887–3892.
- 5 K. Rajeshwar, N. R. de Tacconi and C. R. Chenthamarakshan, *Chem. Mater.*, 2001, **13**, 2765–2782.
- 6 P. H. C. Camargo, K. G. Satyanarayana and F. Wypych, *Mater. Res.*, 2009, **12**, 1–39.
- 7 J. Moczo and B. Pukanszky, *J. Ind. Eng. Chem.*, 2008, **14**, 535–563.



- 8 M. Rahmat and P. Hubert, *Compos. Sci. Technol.*, 2011, **72**, 72–84.
- 9 C. Ingrosso, A. Panniello, R. Comparelli, M. L. Curri and M. Striccoli, *Materials*, 2010, **3**, 1316–1352.
- 10 Y. Wang, *Acc. Chem. Res.*, 1991, **24**, 133–139.
- 11 A. P. Alivisatos, *Science*, 1996, **271**, 933–937.
- 12 S. A. Haque, S. Koops, N. Tokmoldin, J. R. Durrant, J. S. Huang, D. D. C. Bradley and E. Palomares, *Adv. Mater.*, 2007, **19**, 683–687.
- 13 P. Ravirajan, D. D. C. Bradley, J. Nelson, S. A. Haque, J. R. Durrant, H. J. P. Smit and J. M. Kroon, *Appl. Phys. Lett.*, 2005, **86**, 143101.
- 14 P. V. Kamat, *J. Phys. Chem. C*, 2008, **112**, 18737–18753.
- 15 S. M. Choi and H. Awaji, *Sci. Technol. Adv. Mater.*, 2005, **6**, 2–10.
- 16 A. Kar and A. Patra, *J. Phys. Chem. C*, 2009, **113**, 4375–4380.
- 17 P. G. Harrison and M. J. Willet, *Nature*, 1988, **332**, 337–339.
- 18 W. W. Wang, Y. J. Zhu and L. X. Yang, *Adv. Funct. Mater.*, 2007, **17**, 59–64.
- 19 J. Zhu, Z. Lu, S. T. Aruna, D. Aurbach and A. Gedanken, *Chem. Mater.*, 2000, **12**, 2557–2566.
- 20 Y. Wang, X. Jiang and Y. Xia, *J. Am. Chem. Soc.*, 2003, **125**, 16176–16177.
- 21 L. Zhang, H. Zhang, H. Huang, Y. Liu and Z. Kang, *New J. Chem.*, 2012, **36**, 1541–1544.
- 22 J. T. McCue and J. Y. Ying, *Chem. Mater.*, 2007, **19**, 1009–1015.
- 23 J. Pan, J. Li, Z. Yan, B. Zhou, H. Wu and X. Xiong, *Nanoscale*, 2013, **5**, 3022–3029.
- 24 M. Taei, M. Shavakhi, H. Hadadzadeh, M. Movahedi, M. Rahimi and S. Habibollahi, *J. Appl. Electrochem.*, 2015, **45**, 185–195.
- 25 G. An, N. Na, X. Zhang, Z. Miao, S. Miao, K. Ding and Z. Liu, *Nanotechnology*, 2007, **18**, 435707.
- 26 R. K. Selvan, I. Perelshtein, N. Perkas and A. Gedanken, *J. Phys. Chem. C*, 2008, **112**, 1825–1830.
- 27 L. Wang, D. Wang, Z. Dong, F. Zhang and J. Jin, *Nano Lett.*, 2013, **13**, 1711–1716.
- 28 A. Martucci, J. Fick, S.-E. Leblanc, M. Locascio and A. Hache, *J. Non-Cryst. Solids*, 2004, **345**, 639–642.
- 29 D. Berhanu, K. Govender, D. Smyth-Boyle, M. Archbold, D. P. Halliday and P. O'Brien, *Chem. Commun.*, 2006, 4709–4711.
- 30 S. B. Qadri, J. Yang, B. R. Ratna, E. F. Skelton and J. Z. Hu, *Appl. Phys. Lett.*, 1996, **69**, 2205–2207.
- 31 O. M. Ntwaeaborwa, R. E. Kroon, V. Kumar, T. Dubroca, J.-P. Ahn, J.-K. Park and H. C. Swart, *J. Phys. Chem. Solids*, 2009, **70**, 1438–1442.
- 32 P. Ghosh, A. Kar and A. Patra, *J. Appl. Phys.*, 2010, **108**, 113506.
- 33 W. Wu, L. Liao, S. Zhang, J. Zhou, X. Xiao, F. Ren, L. Sun, Z. Dai and C. Jiang, *Nanoscale*, 2013, **5**, 5628–5636.
- 34 A. Kar, A. Datta and A. Patra, *J. Mater. Chem.*, 2010, **20**, 916–922.
- 35 T. Gao and T. Wang, *Chem. Commun.*, 2004, 2558–2559.
- 36 H. M. Rietveld, *Acta Crystallogr.*, 1967, **22**, 151–152; H. M. Rietveld, *J. Appl. Crystallogr.*, 1969, **2**, 65–71; R. A. Young and D. B. Willes, *J. Appl. Crystallogr.*, 1982, **15**, 430–438; L. Lutterotti, P. Scardi and P. Maistrelli, *J. Appl. Crystallogr.*, 1992, **25**, 459–462; R. A. Young, *The Rietveld Method*, Oxford University Press Inc, New York, 1996.
- 37 L. Lutterotti, *Program Maud (version 2.33)*, <http://maud.radiographema.com/>.
- 38 HyperSpy homepage [hyperspy.org](http://hyperspy.org).
- 39 Y. Xu and C. H. Langford, *Langmuir*, 2001, **17**, 897–902.
- 40 J. M. Buriak, P. V. Kamat and K. S. Schanze, *ACS Appl. Mater. Interfaces*, 2014, **6**, 11815–11816.
- 41 S. Sain, A. Kar, A. Patra and S. K. Pradhan, *CrystEngComm*, 2014, **16**, 1079–1090.
- 42 B. E. Warren, *X-ray Diffraction*, Addison-Wesley, Reading, MA, 1969.
- 43 H. Dutta, S. K. Manik and S. K. Pradhan, *J. Appl. Crystallogr.*, 2003, **36**, 260–268.
- 44 D. Rossouw, P. Burdet, F. de la Peña, C. Ducati, B. R. Knappett, A. E. H. Wheatley and P. A. Midgley, *Nano Lett.*, 2015, **15**, 2716–2720.
- 45 A. Kar, S. Kundu and A. Patra, *J. Phys. Chem. C*, 2011, **115**, 118–124.
- 46 G. Xi and J. Ye, *Inorg. Chem.*, 2010, **49**, 2302–2309.
- 47 F. Gu, S. F. Wang, M. K. Lu, G. J. Zhou, D. Xu and D. R. Yuan, *J. Phys. Chem. B*, 2004, **108**, 8119–8123.
- 48 H. Cao, G. Wang, S. Zhang and X. Zhang, *Nanotechnology*, 2006, **17**, 3280–3287.
- 49 Y.-D. Wang, C.-L. Ma, X.-D. Sun and H.-D. Li, *Nanotechnology*, 2002, **13**, 565–569.
- 50 D. Chen and L. Gao, *J. Colloid Interface Sci.*, 2004, **279**, 137–142; Q. Li, X. D. Yuan, G. F. Zeng and S. Q. Xi, *Mater. Chem. Phys.*, 1997, **47**, 239–245; W. Y. Chung, D. D. Lee and B. K. Sohn, *Thin Solid Films*, 1992, **221**, 304–310.
- 51 R. S. C. Smart, W. M. Skinner and A. R. Gerson, *Surf. Interface Anal.*, 1999, **28**, 101–105; M. Takahashi, Y. Ohshima, K. Nagata and S. Furuta, *J. Electroanal. Chem.*, 1993, **359**, 281–286.
- 52 A. Lobo, T. Moller, M. Nagel, H. Borchert, S. G. Hickey and H. Weller, *J. Phys. Chem. B*, 2005, **109**, 17422–17428.
- 53 J. F. Moulder, W. F. Stickle, P. E. Sobol and K. D. Bomben, in *Handbook of X-ray Photoelectron Spectroscopy, Physical Electronics*, ed. J. Chastain, MN, 1995.
- 54 R. S. C. Smart, W. M. Skinner and A. R. Gerson, *Surf. Interface Anal.*, 1999, **28**, 101–105; M. Takahashi, Y. Ohshima, K. Nagata and S. Furuta, *J. Electroanal. Chem.*, 1993, **359**, 281–286.
- 55 S. Chen and W. Liu, *Mater. Chem. Phys.*, 2006, **98**, 183–189.
- 56 L. Cao, H. Wan, L. Huo and S. Hi, *J. Colloid Interface Sci.*, 2001, **244**, 97–101.
- 57 S. Chen and W. Liu, *Mater. Chem. Phys.*, 2006, **98**, 183–189.
- 58 Y. Q. Wang, S. G. Chen, X. H. Tang, O. Palchik, A. Zaban, Y. Koltypin and A. Gedanken, *J. Mater. Chem.*, 2001, **11**, 521–526.





- 59 S.-Y. Chen, H.-D. Tsai, W.-T. Chuang, J.-J. Lee, C.-Y. Tang, C.-Y. Lin and S. Cheng, *J. Phys. Chem. C*, 2009, **113**, 15226–15238.
- 60 A. H. Souici, N. Keghouche, J. A. Delaire, H. Remita, A. Etcheberry and M. Mostafavi, *J. Phys. Chem. C*, 2009, **113**, 8050–8057; M. Yousefi, F. Gholamian, D. Ghanbari and M. Salavati-Niasari, *Polyhedron*, 2011, **30**, 1055–1060; S. Jing, S. Xing and C. Zhao, *Mater. Lett.*, 2008, **62**, 41–43.
- 61 W. W. Wang, Y. J. Zhu and L. X. Yang, *Adv. Funct. Mater.*, 2007, **17**, 59–64.
- 62 O. M. Ntwaeaborwa, R. E. Kroon, V. Kumar, T. Dubroca, J.-P. Ahn, J.-K. Park and H. C. Swart, *J. Phys. Chem. Solids*, 2009, **70**, 1438–1442.
- 63 Y. Feng, L. Li, M. Ge, C. Guo, J. Wang and L. Liu, *ACS Appl. Mater. Interfaces*, 2010, **2**, 3134–3140.
- 64 Y. Yang, D. S. Kim, Y. Qin, A. Berger, R. Scholz, H. Kim, M. Knez and U. Gösele, *J. Am. Chem. Soc.*, 2009, **131**, 13920–13921.
- 65 R. Vinu and G. J. Madras, *J. Indian Inst. Sci.*, 2010, **90**, 189–230.
- 66 Z. Zhang, W. Wang, L. Wang and S. Sun, *ACS Appl. Mater. Interfaces*, 2012, **4**, 593–597.
- 67 S. Khanchandani, S. Kundu, A. Patra and A. K. Ganguli, *J. Phys. Chem. C*, 2013, **117**, 5558–5567.
- 68 R. Bera, S. Kundu and A. Patra, *ACS Appl. Mater. Interfaces*, 2015, **7**, 13251–13259; C. Wang, C. Shao, X. Zhang and Y. Liu, *Inorg. Chem.*, 2009, **48**, 7261–7268.
- 69 A. Kar, S. Sain, S. Kundu, A. Bhattacharyya, S. K. Pradhan and A. Patra, *ChemPhysChem*, 2015, **16**, 1017–1025.
- 70 J. Yu, S. Liu and H. Yu, *J. Catal.*, 2007, **249**, 59–66; J. Yu, G. Wang, B. Cheng and M. Zhou, *Appl. Catal., B*, 2007, **69**, 171–180.
- 71 K. S. W. Sing, D. H. Everett, R. A. W. Haul, L. Moscou, R. A. Pierotti, J. Rouquerol and T. Siemieniowska, *Pure Appl. Chem.*, 1985, **57**, 603–619; E. L. Foletto, S. Battiston, G. C. Collazzo, M. M. Bassaco and M. A. Mazutti, *Water, Air, Soil Pollut.*, 2012, **223**, 5773–5779.
- 72 H.-C. Chiu and C.-S. Yeh, *J. Phys. Chem. C*, 2007, **111**, 7256–7259.
- 73 K. J. A. Raj and B. Viswanathan, *ACS Appl. Mater. Interfaces*, 2009, **1**, 2462–2469.
- 74 Y. C. Zhang, Z. N. Du, K. W. Li, M. Zhang and D. D. Dionysiou, *ACS Appl. Mater. Interfaces*, 2011, **3**, 1528–1537.
- 75 M. T. Uddin, Y. Nicolas, C. Olivier, T. Toupance, L. Servant, M. M. Müller, H.-J. Kleebe, J. Ziegler and W. Jaegermann, *Inorg. Chem.*, 2012, **51**, 7764–7773.

